

# Luminous, pc-scale CO 6–5 emission in the obscured nucleus of NGC 1377

S. Aalto<sup>1</sup>, S. Muller<sup>1</sup>, F. Costagliola<sup>1</sup>, K. Sakamoto<sup>2</sup>, J. S. Gallagher<sup>3</sup>, N. Falstad<sup>1</sup>, S. König<sup>1</sup>, K. Dasyra<sup>4</sup>, K. Wada<sup>5</sup>, F. Combes<sup>6</sup>, S. García-Burillo<sup>7</sup>, L. E. Kristensen<sup>8</sup>, S. Martín<sup>9, 10, 11</sup>, P. van der Werf<sup>12</sup>, A. S. Evans<sup>13</sup>, and J. Kotilainen<sup>14</sup>

(Affiliations can be found after the references)

Received xx; accepted xx

## ABSTRACT

High resolution submm observations are important in probing the morphology, column density and dynamics of obscured active galactic nuclei (AGNs). With high resolution ( $0.''06 \times 0.''05$ ) ALMA 690 GHz observations we have found bright ( $T_B > 80$  K) and compact (FWHM  $10 \times 7$  pc) CO 6–5 line emission in the nucleus of the extremely radio-quiet galaxy NGC 1377. The CO 6–5 integrated intensity is aligned with the previously discovered jet/outflow of NGC 1377 and is tracing the dense ( $n > 10^4$  cm<sup>-3</sup>), hot gas at the base of the outflow. The velocity structure is complex and shifts across the jet/outflow are discussed in terms of jet-rotation or separate, overlapping kinematical components. High velocity gas ( $\Delta v \pm 145$  km s<sup>-1</sup>) is detected inside  $r < 2$ -3 pc and we suggest that it is emerging from an inclined rotating disk or torus of position angle  $PA = 140^\circ \pm 20^\circ$  with a dynamical mass of  $3 \times 10^6 M_\odot$ . This mass is consistent with that of a supermassive black hole (SMBH), as inferred from the  $M - \sigma$  relation. The gas mass of the proposed disk/torus constitutes  $< 3\%$  of the nuclear dynamical mass. In contrast to the intense CO 6–5 line emission, we do not detect dust continuum with an upper limit of  $S(690 \text{ GHz}) \lesssim 2$  mJy. The corresponding, 5 pc, H<sub>2</sub> column density is estimated to  $N(\text{H}_2) < 3 \times 10^{23}$  cm<sup>-2</sup>, which is inconsistent with a Compton Thick (CT) source. We discuss the possibility that CT obscuration may be occurring on small (subparsec) or larger scales. From SED fitting we suggest that half of the IR emission of NGC 1377 is nuclear and the rest (mostly the far-infrared (FIR)) is emerging from larger scales. The extreme radio quietness, and the lack of emission from other star formation tracers, raise questions on the origin of the FIR emission. We discuss the possibility that it is arising from the dissipation of shocks in the molecular jet/outflow or from irradiation by the nuclear source along the poles.

**Key words.** galaxies: evolution — galaxies: individual: NGC 1377 — galaxies: active — galaxies: nuclei — galaxies: ISM — ISM: molecules — ISM: jets and outflows

## 1. Introduction

NGC 1377 is a nearby (21 Mpc ( $1'' = 102$  pc)), lenticular galaxy with a far-infrared (FIR) luminosity of  $L_{\text{FIR}} = 4.3 \times 10^9 L_\odot$  (Roussel et al. 2003). NGC 1377 is the most radio-quiet, FIR-excess galaxy known to date with radio emission being deficient by a factor  $\approx 37$  with respect to normal galaxies (Roussel et al. 2003, 2006). Its nucleus is dust enshrouded (e.g. Spoon et al. 2007) and the source of the FIR luminosity (and cause of its radio deficiency) has remained elusive. A nascent starburst (Roussel et al. 2003, 2006) or a radio-quiet AGN (Imanishi 2006; Imanishi et al. 2009) have been proposed as possible solutions. The energetics of a powerful molecular outflow seem to point towards an AGN (Aalto et al. 2012) and recent ALMA observations revealed that at least part of the outflow is in the form of a peculiar molecular jet. Velocity reversals along the jet may be indications of precession (Aalto et al. 2016). Recently, faint radio emission with a synchrotron spectrum has been detected for the first time, but there appears to be no nuclear X-ray source (Costagliola et al. 2016). The radio detection confirms the extreme FIR-excess of NGC 1377 and that it is well away from the radio-FIR correlation (Helou et al. 1985). Costagliola et al. (2016) use the radio emission to estimate the star formation rate (SFR) finding an  $\text{SFR} < 0.1 M_\odot \text{ yr}^{-1}$ , which is not sufficient to power the observed IR luminosity and to drive the CO outflow. However, even if the evidence in support of a buried AGN is

mounting, the nature of the power source behind the FIR luminosity and the molecular outflow is still not fully understood.

Observations at mid-infrared (mid-IR) wavelengths reveal a compact ( $< 0.''14$ ), high surface brightness source (Imanishi et al. 2011) in the nucleus of NGC 1377. It is not clear if this structure is part of an obscuring torus or disk and if it is opaque enough to absorb X-rays emerging from an accreting supermassive black hole. It is also not understood if and how the obscuring material is linked to the outflowing gas in the jet.

Submm observations of dust continuum are powerful tools in detecting the presence of opaque structures of obscuring dust (e.g. Sakamoto et al. 2008; Wilson et al. 2014). Direct detection on pc-scales of the dust torus around an AGN have, however, remained elusive until recently when Atacama Large Millimeter/submillimeter Array (ALMA) band 9 (690 GHz) observations of the Seyfert galaxy NGC 1068 revealed the presence of the obscuring torus and its turbulent dynamics (García-Burillo et al. 2016; Gallimore et al. 2016). We obtained ALMA band 9 observations to probe the structure and orientation of the intervening dust in the nucleus of NGC 1377 and to determine gas and dust column densities. We also acquired simultaneous CO 6–5 observations to probe the very nuclear pc-scale dynamics of the hot gas.

In Sections 2 and 3 we present the observations and the results. In Section 4 we discuss the nuclear gas excitation, the nuclear dust obscuration and limits to the associated H<sub>2</sub> column densities. We also present a simple two-component model to the

Table 1: CO 6–5 flux densities<sup>a</sup>

Position (J2000)	$\alpha$ : 03:36:39.075 ( $\pm 0.''01$ ) $\delta$ : -20:54:07.06 ( $\pm 0.''01$ )
Peak flux density	$90 \pm 17$ mJy beam <sup>-1</sup>
Flux	
(central beam)	$15 \pm 2.5$ Jy km s <sup>-1</sup> beam <sup>-1</sup>
(whole map)	$40 \pm 7.5$ Jy km s <sup>-1</sup>

a) The position refers to the peak of the integrated CO 6–5 line emission. The Jy to K conversion in the  $0.''06 \times 0.''05$  beam is  $1 \text{ K} = 1.1 \text{ mJy}$ . The peak  $T_B$  is 80 K corresponding to 90 mJy.

dust Spectral Energy Distribution (SED) and discuss the origin of the far-infrared (FIR) emission of NGC 1377. In Section 5 we examine the possible source of the CO 6–5 high-velocity gas, the dynamics of the nuclear disk and the acceleration region of the jet/outflow.

## 2. Observations

Observations of the CO  $J=6-5$  line were carried out with ALMA (with 35 antennas in the array) on 2015 September 25, for 4 minutes on-source (30 minutes in total) and with reasonable atmospheric conditions (precipitable amount of water vapour of  $\sim 0.5$  mm,  $T_{\text{sys}}=600-1200$  K). The phase centre was set to  $\alpha=03:36:39.074$  and  $\delta=-20:54:07.055$  (J2000).

The correlator was set up to cover two spectral windows of 1.875 GHz in spectral mode, one centred at a frequency of  $\sim 690$  GHz to cover the CO  $J=6-5$  line (in the lower side band), and the other centred at 709 GHz to cover the HCN 8–7 line. In addition, two 2 GHz bands were set up in continuum mode.

The bandpass of the individual antennas was derived from the quasar J0522 – 3627. The quasar J0348 – 2749 was observed for complex gain calibration. The absolute flux scale was calibrated using the quasar J0334 – 401.

After calibration within the CASA reduction package (McMullin et al. 2007), the visibility set was imported into the AIPS package for further imaging. The synthesized beam is  $0.''06 \times 0.''05$  ( $6 \times 5$  pc) with Briggs weighting (parameter robust set to 0.5). The on-source observation was short (250 s) - designed to detect a purported high-surface brightness dusty nucleus. The large number of telescopes in the observation ensures a good sampling of the uv-plane despite the short observation ( $B_{\text{max}}=2250$  m,  $B_{\text{min}}=41$  m). However, the recoverable scale is still limited to theoretically  $2.''2$ , but effectively we could not recover structures larger than  $1.''$ .

The resulting data would have a maximum theoretical sensitivity of 9 mJy (dual polarization, Briggs weighting) per beam in a  $20 \text{ km s}^{-1}$  (47 MHz) channel width and in the highest grade weather. Our data set is close to this with an rms of 10 mJy. This means that we are only sensitive to structures with high surface brightness ( $10 \text{ mJy} = T_B = 10 \text{ K}$ ).

## 3. Results

### 3.1. CO 6–5

We detect luminous CO 6–5 emission inside  $r=10$  pc of the NGC 1377 nucleus. The peak flux density is  $90 \pm 17$  mJy beam<sup>-1</sup>,

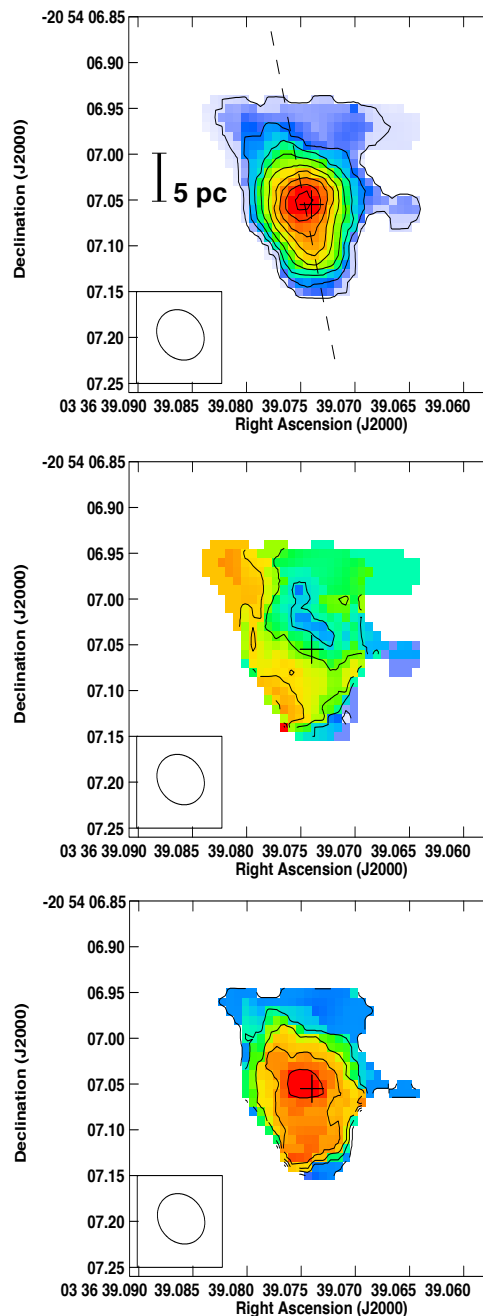


Fig. 1: CO 6–5 moment maps. Top: Integrated intensity (mom0) where contours are  $0.6 \times (1, 4, 7, 10, 13, 16, 19, 22, 25)$  Jy km s<sup>-1</sup> beam<sup>-1</sup>. Colours range from 0 to 15 Jy km s<sup>-1</sup> beam<sup>-1</sup>. The dashed line marks the orientation of the molecular jet (see text for details). Centre: velocity field (mom1) where contours range from  $1690 \text{ km s}^{-1}$  to  $1820 \text{ km s}^{-1}$  in steps of  $10 \text{ km s}^{-1}$ . Bottom: Map of the one-dimensional velocity dispersion (mom2), i.e. the FWHM line width of the spectrum divided by 2.35 for a Gaussian line profile. Contours are  $4.4 \times (1, 3, 5, 7, 9, 11, 13)$  km s<sup>-1</sup> and colours range from 0 to  $66 \text{ km s}^{-1}$ . The cross indicates the position of the 345 GHz continuum peak (see Table 1).

which corresponds to a brightness temperature  $T_B > 80 \text{ K}$  (Tab. 1)<sup>1</sup>.

<sup>1</sup> There are significant effects of decorrelation in our CO 6–5 data implying that the line intensity (and hence  $T_B$ ) may be higher. Here, we use 80 K as a lower limit for the CO 6–5  $T_B$  in the 5 pc beam.

### 3.1.1. Moment maps

The CO 6–5 integrated intensity (moment 0) map, velocity field (moment 1) and dispersion map (moment 2) are presented in Fig. 1. We clipped the moment 0 map at the  $3\sigma$  level. The velocity centroids were determined through a flux-weighted first moment of the spectrum of each pixel, therefore assigning one velocity to a spectral structure. The dispersion was determined through a flux-weighted second moment of the spectrum of each pixel. CO 6–5 flux densities are presented in Tab. 1.

*Moment 0 map* We find a centrally peaked structure with extensions to the north-east and south-west roughly consistent with the orientation of the previously found molecular jet (Aalto et al. 2016). There is also a feature to the north-east with a position angle (PA) of  $30^\circ$  and fainter emission fanning out to the north-west of the nucleus. With a two-dimensional Gaussian fitting we find a full width half maximum (FWHM) source size of  $0.''096 \times 0.''07 (\pm 0.01)$  ( $10 \times 7$  pc). The position angle is  $PA=20^\circ \pm 15^\circ$ .

*Moment 1 and 2 maps* The centroids of the velocity field span  $1690 - 1820 \text{ km s}^{-1}$ . Blue-shifted emission is found to the north, west and south-west of the nucleus, and redshifted velocities are found to the north- and south-east. The velocity field is very complex suggesting multiple overlapping dynamical structures. The dispersion map peaks on the nucleus and has extensions to the south and to the north-east. The peak velocity dispersion is  $\sigma_v=66 \text{ km s}^{-1}$  in the nucleus.

### 3.1.2. High-velocity gas

We integrated the high-velocity emission ( $1500$  to  $1670$  and  $1815$  to  $2000 \text{ km s}^{-1}$ ). We find that the most blue-shifted emission is located in the northern part of the nucleus. The red-shifted emission is found in the southern part of the nucleus and in a  $0.''1$  extension to the south. The peaks of the integrated red- and blue shifted emission are separated by  $0.''05$  ( $5$  pc) with a  $PA=140^\circ \pm 10^\circ$  (see Fig. 2 centre panel).

### 3.1.3. Low-velocity and systemic gas

The low velocity, near-systemic ( $1680 - 1800 \text{ km s}^{-1}$ ) gas is located in the nucleus and in  $10$  pc narrow gas extensions. A velocity field (moment 1) map, where only the brightest emission ( $6\sigma$ ) has been selected, reveal a  $100 \text{ km s}^{-1}$  velocity gradient (from  $1690$  to  $1790 \text{ km s}^{-1}$ ) along a  $0.''08$  axis with a PA of  $120^\circ \pm 10^\circ$  (Fig. 2, right panel). The orientation of the velocity shift is roughly consistent with that of the CO 3–2 disk-like feature (Aalto et al. 2016)).

In Fig. 2 there is also a systemic-velocity feature extending south by  $0.''1$ . A position-velocity (PV) diagram shows this structure as prominent, collimated emission along the north-south axis (Fig. 5 discussed in Sec. 5.2). There is also a narrow, somewhat redshifted ( $1780$ - $1800 \text{ km s}^{-1}$ ), emission component stretching out to the north-east (Fig. 4 discussed in Sec. 5).

## 3.2. Continuum and HCN 8–7

We merged all line-free channels in our observations, but we do not detect any  $690$  GHz continuum with an upper limit of  $2$  mJy ( $1\sigma$ ). No HCN 8–7 emission was detected with limits to the integrated intensity of  $2 \text{ Jy km s}^{-1}$ .

## 4. Nuclear gas and dust properties

### 4.1. Gas excitation

We convolved our CO 6–5 map to the same resolution ( $25$  pc) as that of the CO 3–2 ALMA data of Aalto et al. (2015). The average  $T_B$  for CO 3–2 is  $34$  K, and for CO 6–5 it is  $40$  K resulting in a CO 6–5/3–2 intensity ratio of  $\mathcal{R}$  of  $1.2$ . Such a high value of  $\mathcal{R}$  implies gas densities  $n \gtrsim 10^4 \text{ cm}^{-3}$ , kinetic temperatures  $T_{\text{kin}} > 100$  K, and low to moderate ( $\tau \lesssim 1$ ) line opacities. These properties are similar to those found in the nucleus of the Seyfert galaxy NGC 1068 on spatial scales of  $35$  pc (García-Burillo et al. 2014; Viti et al. 2014).

Using the RADEX (van der Tak et al. 2007) non-LTE radiative transport model, we find that CO column densities of  $N(\text{CO}) = 3 \times 10^{18} \text{ cm}^{-2}$  (for  $\Delta V=150 \text{ km s}^{-1}$ ) and line optical depths near unity, can satisfy  $\mathcal{R}$  and the observed line  $T_B^2$ . For gas number densities  $n \approx 10^4 \text{ cm}^{-3}$ , gas kinetic temperatures are high,  $T_{\text{kin}} > 300$  K and for higher densities  $n \approx 10^5 \text{ cm}^{-3}$  temperatures can be lower,  $T_{\text{kin}} > 100$  K.

For typical CO abundances of  $10^{-5} - 10^{-4}$ , the  $N(\text{CO})$  implies  $\text{H}_2$  column densities of  $N(\text{H}_2)=3 \times 10^{22} - 3 \times 10^{23} \text{ cm}^{-2}$ . This is about one order of magnitude lower than that derived from the CO conversion factor (see Aalto et al. (2016)). If there is a steep nuclear temperature gradient, the value of  $\mathcal{R}$  may be  $\gg 1$  in the inner  $5$  pc to  $< 1$  at a resolution of  $25$  pc. This could potentially allow for higher values of  $N(\text{H}_2)$ , but the weak  $345$  GHz ( $860 \mu\text{m}$ ) continuum in the nucleus found by Aalto et al. (2016) places constraints on  $N(\text{H}_2)$ . In the  $345$  GHz ALMA continuum map we find a total flux of  $2.2$  mJy in a structure with a FWHM size of  $0.''25 \times 0.''09$ . The peak flux is  $1.3$  mJy which corresponds to  $T_B(345 \text{ GHz})=0.3$  K. A lower limit to  $T_d$  is  $34$  K which results in an upper limit to column densities of  $10^{23} \text{ cm}^{-2}$  (for a gas-to-dust ratio of  $100$  and following the prescription in Keene et al. (1982)). If temperatures are indeed  $100$  K the gas column densities drop to  $3 \times 10^{22} \text{ cm}^{-2}$ .

### 4.2. How obscured is NGC 1377?

NGC 1377 is a galaxy with a deep silicate absorption implying a deeply enshrouded nucleus (Spoon et al. 2007) and it has been suggested to belong to a group of galaxies with Compact Obscured Nuclei (CONs). These objects have dust continuum emission that is optically thick down to mm wavelengths (e.g. the LIRG NGC4418 Sakamoto et al. (2013); Costagliola et al. (2013)). CONs have opaque structures on scales of tens of pc with  $N(\text{H}_2)$  in excess of  $10^{25} \text{ cm}^{-2}$ . CONs likely host young dust enshrouded nuclear activity in the form of compact starbursts and/or accreting SMBHs (Aalto et al. 2015). NGC 1377 has also been proposed to harbour young nuclear activity at least partially powered by an accreting SMBH (Aalto et al. 2012, 2016; Costagliola et al. 2016). Its lack of X-ray emission has been suggested to be caused by a large, Compton Thick (CT), column of obscuring dust and gas with  $N(\text{H}_2) > 10^{24} \text{ cm}^{-2}$  (Costagliola et al. 2016).

Compact  $690$  GHz continuum emission is, however, not detected in the nucleus of NGC 1377 with a limit of  $T_B < 2$  K ( $2$  mJy). This is consistent with the faint  $345$  GHz and  $230$  GHz continuum found with ALMA and SMA (Aalto et al. 2012, 2016) on larger scales (see below). For  $T_B(690\text{GHz}) < 2$  K and a dust temperature  $T_d \gtrsim 100$  K, we can estimate an upper limit to

<sup>2</sup> This  $N(\text{CO})$  has an error of a factor of a few. For higher  $N(\text{CO})$ ,  $\mathcal{R}$  quickly drops below unity. For lower  $N(\text{CO})$  it becomes increasingly difficult to find solutions with sufficient line brightness temperature.

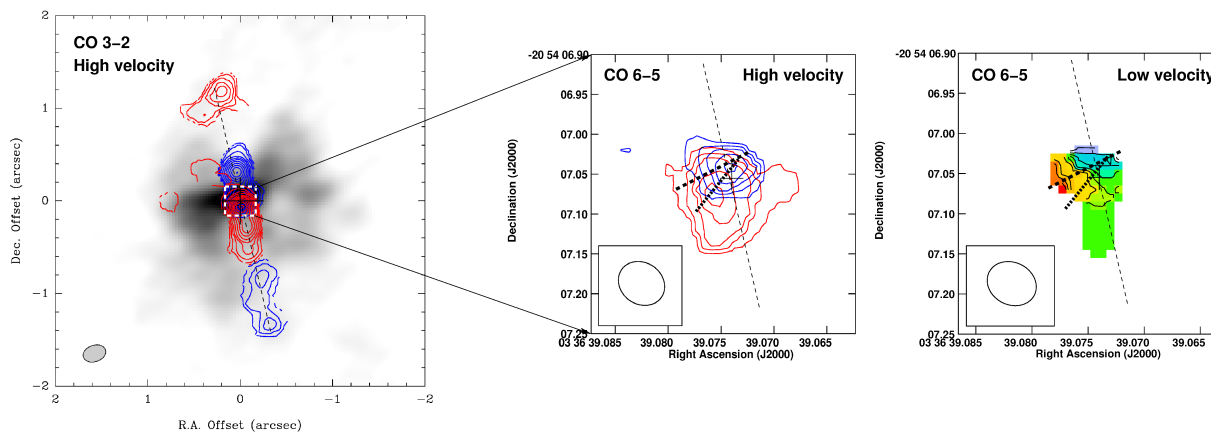


Fig. 2: Left: CO 3–2 integrated intensity image where emission close to systemic velocity ( $1700 - 1760 \text{ km s}^{-1}$ ) is shown in greyscale. The high velocity ( $\pm 80$  to  $\pm 150 \text{ km s}^{-1}$ ) emission from the molecular jet is shown in contours (with the red and blue showing the velocity reversals). The dashed lines indicate the jet axis and the inferred orientation of the nuclear disk. The CO 3–2 beam ( $0.''25 \times 0.''18$ ) is shown as a grey ellipse in the bottom left corner. (This is Fig. 2 in Aalto et al. (2016)). Centre: The high velocity ( $1500$  to  $1670$  and  $1825$  to  $2000 \text{ km s}^{-1}$ ) CO 6–5 emission (see Sect. 5). The contours are  $0.2 \times (1, 3, 5, 7, 9) \text{ Jy km s}^{-1}$ . The beam is 15 times smaller (by surface) than the CO 3–2 beam. Right: The velocity field of the brightest emission (see Sect. 3.1.3) which is close to systemic velocities. The colour scale is ranging from  $1690$  to  $1790 \text{ km s}^{-1}$  and the contours start at  $1690 \text{ km s}^{-1}$  with steps of  $10 \text{ km s}^{-1}$ .

the optical depth  $\tau(690\text{GHz})$  of  $0.02$ . From Keene et al. (1982), the corresponding  $N(\text{H}+\text{H}_2)$  is  $\lesssim 2.4 \times 10^{23} \text{ cm}^{-2}$  in the  $5 \text{ pc}$  ALMA beam. This is consistent with  $N(\text{H}+\text{H}_2)$  derived from the  $345 \text{ GHz}$  continuum emission in a  $0.''25$  aperture (see Sec. 4.1). The limit to  $N(\text{H}+\text{H}_2)$  is also similar to the hydrogen column density estimated from the silicate absorption feature (Roussel et al. 2006; Lahuis et al. 2007). This is a substantial column density, but it does not suggest that the nucleus of NGC 1377 is CT. Not even soft ( $0.5\text{-}2 \text{ keV}$ ) X-rays become strongly absorbed at these column densities (Treister & Urry 2012). However, CT obscuration may occur on smaller or larger scales. Lower resolution *Herschel* observations, for example, find a  $690 \text{ GHz}$  flux of  $200 \text{ mJy}$  (Dale et al. 2014) in contrast to the  $2 \text{ mJy}$  nondetection in our  $5 \text{ pc}$  ALMA beam. The  $690 \text{ GHz}$  flux detected by *Herschel* must therefore have an extended distribution with lower surface brightness. In the following two sections we will discuss the possibility that either foreground obscuration or a small, sub-parsec structure may provide line-of-sight CT obscuration.

#### 4.2.1. Foreground obscuration

In Fig. 3 we present the global IR SED of NGC 1377. We include a two-component fit to the data-points consisting of a *compact* and an *extended* source. We fix the source size of the compact component to  $0.''14$  ( $14 \text{ pc}$ ). This is the upper limit to the high-surface brightness mid-IR ( $18 \mu\text{m}$ ) source found by Imanishi et al. (2011). We also assign it a  $T_d$  of  $100 \text{ K}$ , since Imanishi et al. (2011) derive a mid-IR surface brightness of  $\Sigma_{\text{mid-IR}} > 2.5 \times 10^{13} \text{ L}_\odot \text{ kpc}^{-2}$  implying a  $T_B(18 \mu\text{m}) \gtrsim 100 \text{ K}$ . The limit to the  $690 \text{ GHz}$  flux, if we convolve our ALMA observations to a  $0.''14$  aperture, is  $3.5 \text{ mJy}$ , and we use the  $345 \text{ GHz}$  continuum flux of  $1.3 \text{ mJy}$  (in a  $0.''25$  aperture (Aalto et al. 2015)) as an upper limit to the flux in the  $0.''14$  aperture. The resulting compact SED is shown as the blue curve in Fig. 3. The  $12 \mu\text{m}$  point in the SED is under-predicted suggesting that  $T_d$  is  $> 100 \text{ K}$  or an additional, hotter component.

The extended source, to which we fit the IRAS FIR points and the  $200 \text{ mJy}$  *Herschel*  $690 \text{ GHz}$  continuum data point, does not have a similar size constraint. In general, however, we expect the low- $J$  CO emission to be at least roughly co-existent with

the extended dust component and therefore we selected a size of  $1.''5$  (Aalto et al. 2012, 2016) for the extended component<sup>3</sup>. We find that the compact component has  $N(\text{H}+\text{H}_2)$  in the range of  $10^{22} - 10^{23} \text{ cm}^{-2}$  and to the extended component we can fit values of a few times  $10^{22} \text{ cm}^{-2}$  for dust temperatures around  $40 \text{ K}$ . These combined components will not provide CT obscuration, but we require sensitive, lower resolution ALMA observations to search for the potential presence of colder large-scale emission. The  $345 \text{ GHz}$  ALMA observations hint at the presence of a disk-like  $0.''8$  continuum feature with very low surface brightness. This structure should be explored in future observations.

#### 4.2.2. Is there a subparsec Compton thick core?

Alternatively, a CT source may be significantly smaller than our ALMA  $5 \text{ pc}$  beam. A simple model with  $N(\text{H}_2) = 1 \times 10^{25} \text{ cm}^{-2}$  and constrained to have an upper limit to its  $690 \text{ GHz}$  continuum flux of  $2 \text{ mJy}$  gives corresponding maximum sizes of an opaque dust structure in the NGC 1377 nucleus. We can model the  $690 \text{ GHz}$  flux from such an opaque structure through  $S(690 \text{ GHz}) = 10^{-26} B_\nu(T) \pi r^2 / D^2 (1 - \exp(-\tau))$  (where  $D$  is the distance to NGC 1377,  $r$  is the radius of the dust structure,  $B_\nu(T)$  is the Planck function). Thus, for an upper limit on  $S(690)$ , we have  $r = \sqrt{(0.002/1e26/B_\nu(T)/\pi D^2/(1 - \exp(-\tau)))}$ . Maximum sizes for  $r$  range from  $0.7$  to  $0.2$  for dust temperatures ranging from  $100\text{-}700 \text{ K}$ . The dust sublimation radius is  $0.02 - 0.05 \text{ pc}$  from an AGN of luminosity  $10^{43} \text{ erg/s}$  (Netzer 2015). An obscuring screen as small as  $r = 0.2 \text{ pc}$  may therefore be possible and would not be detected with the resolution and sensitivity of the ALMA observations presented here.

#### 4.3. Origin of the FIR luminosity

The detection of faint radio emission with a synchrotron spectrum by Costagliola et al. (2016) suggests that NGC 1377 is not

<sup>3</sup> The sensitivity of the  $690 \text{ GHz}$  ALMA observations presented here declines with increasing beam-size and in a  $1.''8$  beam there are only very few baselines left and the sensitivity is effectively  $50 \text{ mJy}$ . There is therefore nothing in our observations that contradict that the *Herschel* flux can be distributed on the scales inferred from the CO observations.

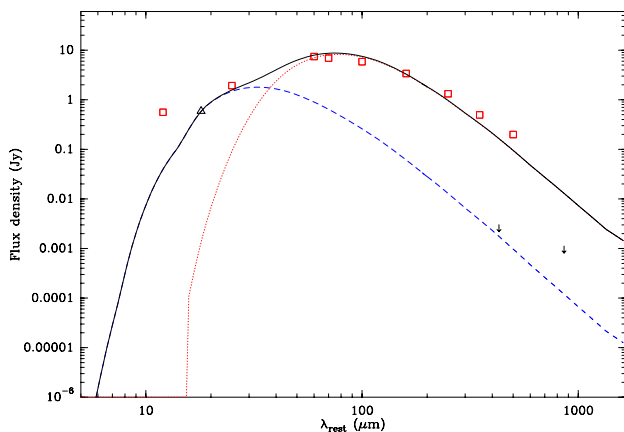


Fig. 3: An example of a two-component model for the dust SED. It consists of a hot compact ( $0.''14$ ) component with  $T_d=100$  K and an extended ( $1.''5$ ) component with  $T_d=40$  K. For a gas-to-dust ratio the  $H_2$  column densities are  $N(H_2)=3 \times 10^{22}$  and  $2 \times 10^{22}$  respectively. Luminosities are  $1.1 \times 10^9 L_\odot$  for the compact component and  $2.2 \times 10^9 L_\odot$  for the extended one. The observed SED points are marked as red squares and were taken from <http://ned.ipac.caltech.edu/forms/photo.html>.

powered by a buried nascent starburst. This is consistent with the discovery of a molecular jet in NGC 1377 which suggests that its nucleus is powered by a single accreting object, an AGN. In addition, based on their IR AGN-Starburst diagnostic diagrams, Dale et al. (2014) suggest that NGC 1377 is located away from "actively star forming" and into the region with a significant AGN contribution (near the 75% contribution line).

We have previously estimated the mass of the buried SMBH to  $\approx 1.5 \times 10^6 M_\odot$  (Aalto et al. 2012). The Eddington luminosity of a  $10^6 M_\odot$  SMBH is about  $5 \times 10^{10} L_\odot$ . If all the mid-IR luminosity ( $1 \times 9 L_\odot$  to  $4 \times 9 L_\odot$ ) is due to an accreting SMBH, we find it is growing at a rate of 1% - 10% Eddington which would place it in the quasar-mode of accretion<sup>4</sup>. Alternatively, the mid-IR emission may be originating from an extremely radio-quiet nuclear starburst as suggested by Roussel et al. (2006). The molecular jet would then be powered by an SMBH accreting at a substantially lower Eddington rate.

In our models above, the FIR emission cannot be emerging from the same compact structure as the mid-IR. We inferred a source size of  $1.''5$  to fit with the CO emission, but we stress that we do not know the extent of the FIR emission. We require a lower resolution and higher sensitivity image to locate the missing 690 GHz emission and to solve the mystery of what processes generate the FIR emission of NGC 1377. However, it is reasonable to assume that at least part of the FIR and CO ( $J=2-1$ ,  $3-2$ ) emission coexist and we note that most of the CO  $2-1$  and  $3-2$  emission of NGC 1377 appears to be associated with a molecular jet/outflow (Aalto et al. 2012, 2016). The lack of star formation indicators imply that a substantial part of the FIR emission is not associated with dust heated by massive stars. An alternative is that the dust is heated by mechanical interactions in the outflow, and/or by photons escaping from the AGN along

<sup>4</sup> Note that this discussion assumes that the IR emission is absorbed and reradiated uv and X-ray emission from an efficiently accreting SMBH. An alternative possibility is an AGN in low-accretion radio-mode. It may generate a radio jet which is shock heating gas and dust in the nucleus. This scenario would be unusual but deserves future consideration - for example through searching for hard X-ray emission associated with hard-state low accretion mode.

the poles. The old stellar component may also contribute to the heating of the dust and gas.

## 5. Nuclear dynamics

The observations were primarily designed to locate a (purported) high-surface brightness nuclear continuum source with associated compact CO 6–5 emission. In addition, observations of Galactic disk-outflow objects show that the CO 6–5 emission is often associated with current shock regions (while lower- $J$  emission such as CO 3–2 more reflects conditions in the larger-scale environment) (Yıldız et al. 2015). Thus, our CO 6–5 observations may not give us a complete picture of the dynamics in the nuclear region. However, they provide important information on the very inner kinematics and how the activity is interacting with its surroundings. The PA of the integrated CO 6–5 emission  $20^\circ \pm 15^\circ$  implies that it is largely aligned with the jet/outflow and not dominated by a rotating torus. CO 6–5 emission from the base of the jet/outflow shows that the gas is dense ( $> 10^4 \text{ cm}^{-3}$ ) and high brightness temperatures reveal that it is also warm. Possible heating mechanisms include shocks in the outflowing gas or from instabilities, and/or heating by radiation from the AGN.

The gas at the highest velocities (that we are sensitive to) is found very close ( $r=2-3$  pc) to the nucleus. The velocity shift is  $145 \text{ km s}^{-1}$ , which is similar to the shift of  $150 \text{ km s}^{-1}$  found previously for the lower resolution CO 3–2 data. However, there the maximum velocity occurred further from the nucleus ( $0.''25=25$  pc) along a collimated jet-structure (Aalto et al. 2016). The velocity reversals along the CO 3–2 jet (see Fig. 2, left panel) are suggested to be caused by jet precession (Aalto et al. 2016). Below we discuss if the CO 6–5 high velocity gas is associated with the rotation of a nuclear disk or with the jet/outflow.

### 5.1. The high velocity gas

*Disk* If the velocity shift is due to rotation in a disk, the projected rotational velocity is  $73 \text{ km s}^{-1}$ . The peaks are separated by 5 pc and, assuming an edge-on disk, the dynamical mass<sup>5</sup> is  $M_{\text{dyn}} = 3 \times 10^6 M_\odot$  inside  $r=2.5$  pc. This is close to the SMBH mass of  $1.5 \times 10^6 M_\odot$  inferred from the  $M-\sigma$  relation (Aalto et al. 2012). The PA between the peaks of  $140^\circ \pm 10$  is shifted by  $20^\circ$  from that of the lower velocity rotating structure, but it is within the error bars of both PA. Thus, it is possible that the high velocity peaks (at least partially) may stem from a Keplerian disk. In Fig. 4 we show the Keplerian tracks of three different compact masses overlaid on the major axis PV diagram of the high velocity emission. Comparing the tracks to the data we see that the expected high velocity cusp in the center is missing. Deeper observations are required to determine if this is a sensitivity issue or if there is no nuclear gas with velocities  $> 100 \text{ km s}^{-1}$ . There is also CO 6–5 emission at forbidden velocities indicating non-circular motions in the form of turbulence, instabilities and/or outflowing gas (García-Burillo et al. 2016). Within the errors, the data allows for either a single SMBH or a combination of a SMBH and a compact nuclear stellar cluster (see e.g. cluster rotation curves in Stone & Ostriker (2015)).

We can obtain estimates to the disk gas inside 5 pc by adopting the limit to  $N(H_2)$  derived in Sec.4.2 and assume that it fills the beam, which leads to  $M_{\text{gas}} \lesssim 10^5 M_\odot$ . However, since there may also be emission from the outflow in the inner beam, a

<sup>5</sup> A simple estimate of the dynamical mass is  $M_{\text{dyn}} = RV_{\text{rot}}^2/G$ , where  $V_{\text{rot}}$  is the rotation speed.



limit to  $M_{\text{gas}}$  can also be obtained through inferring an edge-on disk with thickness  $h=r/2$  and using the limit to  $N(\text{H}_2)$  then  $M_{\text{gas}} \lesssim 2 \times 10^4 M_{\odot}$ . In any case, the gas mass is significantly lower than the dynamical mass ( $<3\%$ ), which again suggests similar properties to those of the non self-gravitating gas torus of NGC 1068 (García-Burillo et al. 2016).

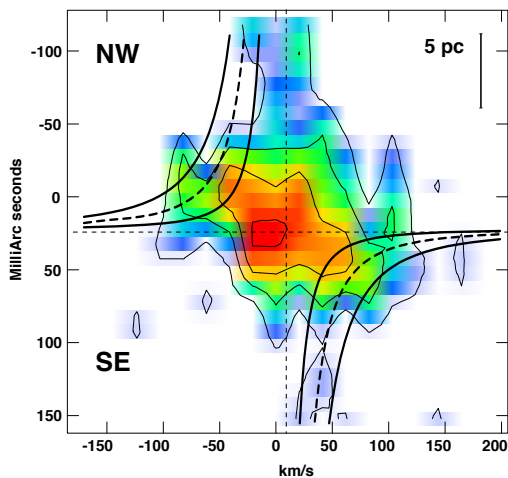


Fig. 4: CO 6–5 PV diagrams. Top: PA=135° close to the major axis of the nuclear disk. The curves show the Keplerian rotation curves of a:  $10^6$ ,  $3 \times 10^6$  and  $6 \times 10^6 M_{\odot}$  SMBH. Bottom: Cut perpendicular (PA=45°) to the nuclear disk. The contour levels are  $25 \times (1, 2, 3) \text{ mJy beam}^{-1}$ . Colours range from 25 to  $90 \text{ mJy beam}^{-1}$ . A velocity of  $0 \text{ km s}^{-1}$  corresponds to  $1743 \text{ km s}^{-1}$ .

**Jet/outflow** The previously found molecular jet has a symmetry axis of  $\approx 11^\circ$  and was suggested to precess with an angle  $\theta=10^\circ - 25^\circ$ . The simple precessing jet model proposed in Aalto et al. (2016) predicts that velocities, after peaking at a distance  $\pm 25 \text{ pc}$ , decrease closer to the nucleus. In the CO 6–5 data there are no strong signatures ( $>3\sigma$ ) of high velocity gas at  $\pm 0.''25$ . This may be a sensitivity issue and/or that the gas temperature and density is only high enough to excite the CO 3–2 line 25 pc along the jet - not CO 6–5. The PA of  $140^\circ \pm 10$  of the nuclear CO 6–5 high-velocity gas is also inconsistent with it being associated with gas along the jet. However, luminous CO 6–5 emission at velocities closer to systemic is detected along the jet (see discussion in Sec 5.2).

We tentatively conclude that the most likely origin of the nuclear CO 6–5 high velocity gas is in a rotating, inclined disk.

However, we cannot exclude that the jet behaviour has changed close to the nucleus or that it has turned off. We may be resolving the jet or the high velocity gas is emerging from another outflow structure.

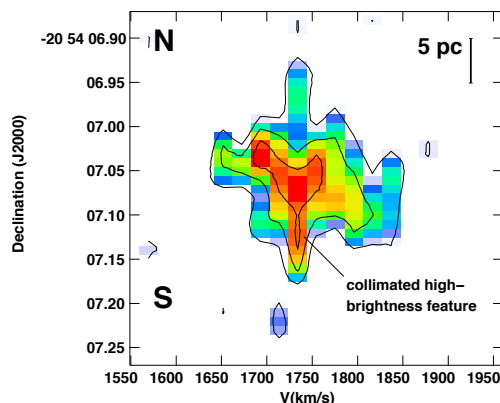


Fig. 5: Position-velocity (PV) diagram along the north-south axis. The contour levels are  $25 \times (1, 2, 3) \text{ mJy beam}^{-1}$ . Colours range from 25 to  $90 \text{ mJy beam}^{-1}$ .

## 5.2. Jet dynamics

A component that would fit the jet-precession model is the bright, narrow feature emerging from the nucleus in the north-south direction (Fig. 5). It is found at systemic velocities, and would be consistent with a scenario where the jet has precessed away from its symmetry axis and is now at its maximum angle away from the symmetry axis. In this case, the jet precession angle would be close to  $\theta=10^\circ$ . The high CO 6–5 brightness temperature of (at least the southern) collimated feature may indicate shock-heating by the jet-interaction. Note that if jet precession is caused by the warping of the nuclear disk (see discussion in Aalto et al. (2016)) then the inner disk should have a PA close to  $90^\circ$  which appears to be inconsistent with the PA of the nuclear disk found above. However, the precession may be governed by the accretion disk which would be much smaller than 5 pc.

There are also other (somewhat fainter) narrow jet-like features in the map. One is a structure emerging to the north-east at PA=45° and which may have a counterpart to the south-west. We can see it as a redshifted component extending 20 pc along the north-eastern part of the minor axis (right panel in Fig. 4). It is not clear if this is a separate component - or if all (seemingly) collimated features are part of the same outflow. In our previous CO 3–2 observations, we did not resolve the high velocity jet in our  $0.''25$  beam. Even though a radio jet may have a very narrow width and could be unresolved also by our CO 6–5 5 pc beam, it would interact with its surroundings resulting in a wider structure.

### 5.2.1. A disk-wind?

It is also possible that the jet formation is strongly linked to the molecular disk in the form of a disk-wind (see Gallimore et al. (2016) for a discussion of a potential disk-wind scenario for NGC 1068). In this case we may expect to see remnants of the disk rotation in the outflowing gas as a velocity gradient across the jet (e.g. Smith & Rosen 2007; Launhardt et al. 2009). Jet-rotation is an efficient way of removing angular momentum and solving the problem of extracting the angular momentum of the

circumnuclear gas. Jet/outflow rotation may also be driven by MHD shocks in helical magnetic fields (e.g. Fendt 2011). Jet rotation structures dissipate quickly and are expected to be found close to the nucleus.

There is a velocity shift across the jet to the north and south of about  $150 \text{ km s}^{-1}$ , but it is not clear if this is indeed due to jet rotation or to overlapping, separate dynamical components stemming from other processes. There may also be contamination from the disk rotation near the nucleus. In addition, a very thin radio-jet pushing itself through a dense medium may result in gas being accelerated in opposite directions, perpendicular to the jet (see e.g. discussion in Dasyra et al. (2015)). To fully explore the link between the disk and the jet/outflow high-resolution observations at multiple frequencies are required.

## 6. Conclusions

We have used ALMA to image the CO 6–5 emission, and put limits on the 690 GHz continuum in the nucleus of the extremely radio-quiet lenticular galaxy NGC 1377 with a resolution of  $6 \times 5 \text{ pc}$ . We find luminous, compact ( $10 \times 7 \text{ pc}$ ) CO 6–5 emission from hot ( $T_{\text{kin}} \gtrsim 100 \text{ K}$ ) molecular gas. The CO 6–5 integrated intensity is aligned with the previously discovered jet/outflow of NGC 1377 and is also tracing the dense, hot gas at the base of the outflow. Collimated, 10 pc long, high brightness features extend from the nucleus and are likely associated with the jet. The velocity structure is complex and a gradient across the jet may be a signature of rotation, alternatively the gradient is caused by separate, overlapping dynamical components.

High velocity gas ( $\Delta v \pm 145 \text{ km s}^{-1}$ ) is detected inside  $r < 2\text{--}3 \text{ pc}$  and we suggest that it is emerging from an inclined rotating disk or torus of PA  $140^\circ \pm 20^\circ$  and a dynamical mass of  $3 \times 10^6 M_\odot$ . This mass is consistent with that of a supermassive black hole (SMBH), as inferred from the  $M - \sigma$  relation. The gas mass of the proposed disk/torus constitutes  $< 3\%$  of the nuclear dynamical mass. In contrast to the intense CO 6–5 line emission, we do not detect dust continuum with an upper limit of  $S(690 \text{ GHz}) \lesssim 2 \text{ mJy}$ . The corresponding 5 pc  $\text{H}_2$  column density is estimated to  $N(\text{H}_2) < 3 \times 10^{23} \text{ cm}^{-2}$  which is inconsistent with a Compton Thick (CT) source (with  $N(\text{H}_2) > 10^{24} \text{ cm}^{-2}$ ). CT obscuration may instead occur in a much smaller, subparsec, structure undetected by ALMA. CT obscuration stemming from larger scale structures seems inconsistent with current data. From SED fitting we suggest that half of the IR emission of NGC 1377 is nuclear and the rest (mostly the far-infrared (FIR)) is emerging from larger scales. The extreme radio quietness, and the lack of other star formation tracers, raise questions on the origin of the FIR emission. We discuss the possibility that it is arising from the dissipation of shocks in the molecular jet/outflow or from irradiation by the nuclear source along the poles. If the FIR emission is associated with star formation in a disk, it is for some reason not producing radio emission.

*Acknowledgements.* This paper makes use of the following ALMA data: ADS/JAO.ALMA#2012.1.00900.S. ALMA is a partnership of ESO (representing its Member States), NSF (USA) and NINS (Japan), together with NRC (Canada) and NSC and ASIAA (Taiwan), in cooperation with the Republic of Chile. The Joint ALMA Observatory is operated by ESO, AUI/NRAO and NAOJ. We thank the Nordic ALMA ARC node for excellent support. SA acknowledges support from the Swedish National Science Council grant 621-2011-4143. F.C. acknowledges support from Swedish National Science Council grant 637-2013-7261 KS was supported by grant MOST 102-2119-M-001-011-MY3 SGB thanks support from Spanish grant AYA2012-32295.

## References

- Aalto, S., Costagliola, F., Muller, S., et al. 2016, *A&A*, 590, A73  
Aalto, S., Costagliola, S. M. F., Gonzalez-Alfonso, E., et al. 2015, *ArXiv e-prints* [arXiv:1504.06824]  
Aalto, S., Muller, S., Sakamoto, K., et al. 2012, *A&A*, 546, A68  
Costagliola, F., Aalto, S., Sakamoto, K., et al. 2013, *A&A*, 556, A66  
Costagliola, F., Herrero-Illana, R., Lohfink, A., et al. 2016, *A&A*, 594, A114  
Dale, D. A., Helou, G., Magdis, G. E., et al. 2014, *ApJ*, 784, 83  
Dasyra, K. M., Bostrom, A. C., Combes, F., & Vlahakis, N. 2015, *ArXiv e-prints* [arXiv:1503.05484]  
Fendt, C. 2011, *ApJ*, 737, 43  
Gallimore, J. F., Elitzur, M., Maiolino, R., et al. 2016, *ApJ*, 829, L7  
García-Burillo, S., Combes, F., Ramos Almeida, C., et al. 2016, *ApJ*, 823, L12  
García-Burillo, S., Combes, F., Usero, A., et al. 2014, *A&A*, 567, A125  
Helou, G., Soifer, B. T., & Rowan-Robinson, M. 1985, *ApJ*, 298, L7  
Imanishi, M. 2006, *AJ*, 131, 2406  
Imanishi, M., Imase, K., Oi, N., & Ichikawa, K. 2011, *AJ*, 141, 156  
Imanishi, M., Nakanishi, K., Tamura, Y., & Peng, C. 2009, *AJ*, 137, 3581  
Keene, J., Hildebrand, R. H., & Whitcomb, S. E. 1982, *ApJ*, 252, L11  
Lahuis, F., Spoon, H. W. W., Tielens, A. G. G. M., et al. 2007, *ApJ*, 659, 296  
Launhardt, R., Pavlyuchenkov, Y., Gueth, F., et al. 2009, *A&A*, 494, 147  
McMullin, J. P., Waters, B., Schiebel, D., Young, W., & Golap, K. 2007, in *Astronomical Society of the Pacific Conference Series*, Vol. 376, *Astronomical Data Analysis Software and Systems XVI*, ed. R. A. Shaw, F. Hill, & D. J. Bell, 127  
Netzer, H. 2015, *ARA&A*, 53, 365  
Roussel, H., Helou, G., Beck, R., et al. 2003, *ApJ*, 593, 733  
Roussel, H., Helou, G., Smith, J. D., et al. 2006, *ApJ*, 646, 841  
Sakamoto, K., Aalto, S., Costagliola, F., et al. 2013, *ApJ*, 764, 42  
Sakamoto, K., Wang, J., Wiedner, M. C., et al. 2008, *ApJ*, 684, 957  
Smith, M. D. & Rosen, A. 2007, *MNRAS*, 378, 691  
Spoon, H. W. W., Marshall, J. A., Houck, J. R., et al. 2007, *ApJ*, 654, L49  
Stone, N. C. & Ostriker, J. P. 2015, *ApJ*, 806, L28  
Treister, E. & Urry, C. M. 2012, *Advances in Astronomy*, 2012, 516193  
van der Tak, F. F. S., Black, J. H., Schöier, F. L., Jansen, D. J., & van Dishoeck, E. F. 2007, *A&A*, 468, 627  
Viti, S., García-Burillo, S., Fuente, A., et al. 2014, *A&A*, 570, A28  
Wilson, C. D., Rangwala, N., Glenn, J., et al. 2014, *ApJ*, 789, L36  
Yıldız, U. A., Kristensen, L. E., van Dishoeck, E. F., et al. 2015, *A&A*, 576, A109
- 
- <sup>1</sup> Department of Earth and Space Sciences, Chalmers University of Technology, Onsala Observatory, SE-439 92 Onsala, Sweden  
e-mail: saalto@chalmers.se
  - <sup>2</sup> Institute of Astronomy and Astrophysics, Academia Sinica, PO Box 23-141, 10617 Taipei, Taiwan
  - <sup>3</sup> Department of Astronomy, University of Wisconsin-Madison, 5534 Sterling, 475 North Charter Street, Madison WI 53706, USA
  - <sup>4</sup> Department of Astrophysics, Astronomy & Mechanics, Faculty of Physics, University of Athens, Panepistimiopolis Zografos 15784, Greece
  - <sup>5</sup> Kagoshima University, Kagoshima 890-0065, Japan
  - <sup>6</sup> Observatoire de Paris, LERMA (CNRS:UMR8112), 61 Av. de l'Observatoire, 75014 Paris, France
  - <sup>7</sup> Observatorio Astronómico Nacional (OAN)-Observatorio de Madrid, Alfonso XII 3, 28014-Madrid, Spain
  - <sup>8</sup> Centre for Star and Planet Formation, Niels Bohr Institute and Natural History Museum of Denmark, University of Copenhagen, Øster Voldgade 5-7, DK-1350 Copenhagen K, Denmark
  - <sup>9</sup> European Southern Observatory, Alonso de Córdova 3107, Vitacura, Santiago, Chile
  - <sup>10</sup> Joint ALMA Observatory, Alonso de Córdova 3107, Vitacura, Santiago, Chile
  - <sup>11</sup> Institut de Radio Astronomie Millimétrique (IRAM), 300 rue de la Piscine, Domaine Universitaire de Grenoble, 38406 St. Martin d'Hères, France
  - <sup>12</sup> Leiden Observatory, Leiden University, 2300 RA, Leiden, The Netherlands
  - <sup>13</sup> University of Virginia, Charlottesville, VA 22904, USA, NRAO, 520 Edgemont Road, Charlottesville, VA 22903, USA
  - <sup>14</sup> Finnish Centre for Astronomy with ESO (FINCA), University of Turku, Väisälantie 20, FI-21500 Kaarina, Finland